Real-Time MOSFET Condition Monitoring for Variable Mission Profiles With a Dual Extended Kalman Filter

Martijn Deckers, Leander Van Cappellen, Jens Moschner, Michaël Daenen, and Johan Driesen

***Abstract*—The paper proposes a methodology to detect real-time power MOSFET degradation, in variable mission profile applications, using externally measurable electrical parameters. This complements the work done for fixed operation conditions in current literature. To achieve this, the damage and temperature sensitive drain to source resistance is accompanied with a gate resistance measurement only sensitive to temperature. Together, they allow for the detection of, and the distinction between, bond wire and die attach solder layer degradation. A Dual Extended Kalman filter is used to filter the measurement data and to estimate the change in thermal model. The paper shows the measurement circuits together with proof of concept lab results in a solar photovoltaic use-case. The main aim is to show that the resistance measurement can be compensated for mission profile temperature variations and that the thermal resistance can be estimated, reflecting bond wire and die attach solder layer degradation.**

***Index Terms*—Condition monitoring, Kalman filtering, Fault diagnosis, Temperature measurement, Photovoltaic power systems.**

I. Introduction

A. Motivation

Reliability is a substantial aspect within the field of power electronic systems and a lot of study is devoted to facilitate the improvement thereof. Semiconductor switching devices often show to be one of the failure prone components limiting the reliability of the entire power conversion system [1]. Generally, two main approaches exist to elevate the reliability of a system. The first approach aims to incorporate reliability in the design phase. Different designs can be compared by estimating the lifetimes with one of the techniques proposed in literature [2], [3]. After careful analysis, a trade off can be made and the most optimal design can be chosen. A second approach focuses on the operation phase and involves condition monitoring which can be adopted on both new and existing systems. Once the status of the switching devices within an operational converter is known, maintenance can be planned accordingly or even dedicated control methods can be adopted, relieving stress from the most critical components [4], [5]. This paper will focus on the second reliability improvement approach, developing a condition monitoring methodology.

Martijn Deckers, Jens Moschner, and Johan Driesen are with ESAT/ELECTA KU Leuven, Kasteelpark Arenberg 10, 3001 Heverlee, Belgium and EnergyVille, Thor Park 8301, 3600 Genk, Belgium (email: martijn.deckers@kuleuven.be, jens.moschner@kuleuven.be, johan.driesen@kuleuven.be). Leander Van Cappellen, and Michaël Daenen are with IMO-IMOMEC Hasselt University, Wetenschapspark 1, 3590 Diepenbeek, Belgium and EnergyVille, Thor Park 8301, 3600 Genk, Belgium (email: leander.vancappellen@uhasselt.be, michael.daenen@uhasselt.be).
This work has been supported by Flanders Innovation & Entrepreneurship and Flux50 under project DAPPER, HBC.2020.2144. Martijn Deckers is funded by a PhD grant from the Research Foundation Flanders (FWO), 1S87522N.

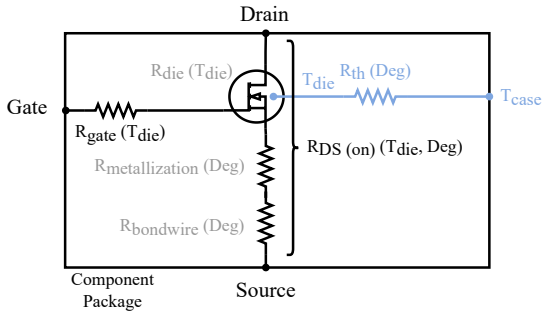

Fig. 1: Visual representation of the TSEP and DSEP used in the condition monitoring methodology.

B. Background

1) Damage and temperature sensitive parameters: Condition monitoring is often done by externally measuring electrical parameters that directly or indirectly reflect the operational conditions of the components. Generally two parameter categories are defined based on the sensitivity, either to the component temperature or the level of damage present in the component. This distinction is not always strict as most are both temperature sensitive electrical parameters (TSEP) and damage sensitive electrical parameters (DSEP) [6]. Fig. 1 gives a graphical representation of the different component parameters and their dependencies on the die temperature T_{die} and degradation (Deg). The degradation of the bondwire and aluminum metallization is mainly notable in the electrical resistance of the bondwire $R_{bondwire}$ and the contact resistance with the metallization layer $R_{metallization}$. This results in an increased drain to source on-resistance $R_{DS(on)}$, as the bondwires and metallization layer are series elements comprising this resistance. $R_{DS(on)}$ is also temperature sensitive as the combined channel, accumulation layer and drift region resistance R_{die} is temperature sensitive. Solder layer delamination mainly affects the thermal performance of the component due to an increase in the thermal resistance R_{th}. The electrical resistance is mostly assumed to be unaffected as the electrical contact surface remains very large in comparison with the bond wire diameter. Notwithstanding, the electrical resistance is indirectly effected by an increase in temperature when the thermal path deteriorates [7]–[9]. The internal gate resistance R_{gate} is not sensitive to package level degradation as the power flow through the gate bondwire is limited. As a result R_{gate} is only sensitive to temperature if no die level degradation occurs [10].

2) Condition monitoring: In current literature on condition monitoring, often one of two routes is taken. The first approach aims to estimate the junction temperature of the switching device as accurate as possible. An overview of the TSEP that can be used is given in [11],

TABLE I: Summary of the existing online switching device condition monitoring methods.

Ref	Component	Package type	Method	Varying profile	Temperature estimate	Degradation detection	Failure mode	Noise filter	No recalibration	No training	No model	Computation resources	Material resources
[12]	SiC MOSFET	Power module	Parameter	✓	✓	✗	✗	✗	✗	✓	✓	Negligible	-
[13]	Si IGBT	Power module	Kalman filter	✓	✓	(✓)	✗	✓	✗	✓	✗	-	-
[14]	SiC MOSFET	Power module	EKF	✓	✓	(✓)	✗	✓	✗	✓	✗	- -	-
[15]	SiC MOSFET	Power module	Neural net	✓	✓	✗	✗	✓	✗	✗	✓	-	- - -
[16]	Si IGBT	Power module	Parameter	✗	✗	✓	✗	✗	✓	✓	✓	Negligible	- -
[17]	Si MOSFET	TO220	PSO	(✓)	✗	✓	✗	✓	✓	✓	✗	- -	(- -)
[18]	Si MOSFET	TO220	GPR/ EKF/PF	✗	✗	✓	✗	✓	✓	✓	✓	- -	-
[19]	Si MOSFET	TO220	Kalman filter	✗	✗	✓	✗	✓	✓	✓	✓	-	-
[20]	Si MOSFET	?	EKF	✗	✗	✓	✗	✓	✓	✓	✗	- -	(- -)
	Si MOSFET	TO220	DEKF	✓	✓	✓	✓	✓	✓	✓	✗	- - -	- -

[12]. In this process, the possibility of degradation is neglected or a re-calibration of the TSEP is proposed at certain time intervals. Often, a direct conversion from the measured parameter to the junction temperature leads to an unacceptable amount of noise in the estimate. This can be solved by filtering the measurement, e.g. with a Kalman filter, provided that the thermal model is known [13], [14]. Multiple measurements can also be combined into one, more robust die temperature estimate, using the same filter based methodology or more data driven concepts e.g. neural networks as is done in [15].

The second approach which is often taken in literature, is the evaluation of degradation levels for constant mission profiles. Measurement of the DSEP in this case, translates immediately to the experienced damage, allowing to make abstraction of the very limited temperature variations [16]. Also here, filtering might be needed, which can be established by using an electrical or thermal model as shown in [17]. It is also possible to propose a degradation profile and fit it to the observed data using Kalman filters, Particle Filters (PF) or other data driven techniques such as neural networks, Particle Swarm Optimization (PSO) and Gaussian Process Regression (GPR) as is demonstrated in [18]–[21]. This makes use of the knowledge that degradation can only increase over time. A summary of the available literature on these two approaches is given in Table I.

C. Contribution

1) Problem statement: In fixed mission profile applications, both methodologies allow to assess degradation. Every deviation from the reference condition, either in temperature or damage level, has to be caused by a change in component parameters, hence, degradation. This can for example be used in power cycling setups, aiming to follow the progress of degradation under the application of constant power or temperature cycles [22]. For applications with slightly varying mission profiles, it might be acceptable to ignore the temperature dependencies or set the degradation thresholds large enough to ensure that only severe degradation triggers an alarm [23]. For other applications, such as renewable energy converters with highly varying mission profiles, the techniques in Table I are not suited. It is impossible to distinguish variations caused by normal temperature fluctuations from actual degradation. Hence, a new integrated technique is needed, capable of estimating the temperature and damage profile simultaneously. The temperature estimation approaches in Table I, using a Kalman filter, already allows to get an indication that damage might be present. An increasing filter residual indicates that the used model is becoming a less accurate representation of the actual physical system, implying that degradation is occurring. Hence, the check-marks between brackets. This, however, is not yet a clear representation of the magnitude in damage and which specific failure mode is triggered.

2) Solution: This paper aims to bridge that gap by proposing an actual dual estimation, employing two condition monitoring measurements. The first measurement $R_{DS(on)}$ is sensitive to both degradation and temperature while the second measurement R_{gate} is only sensitive to temperature. Data driven techniques could be used to relate these measurements to the junction temperature and degradation, however, lots of training data would be needed. This is inconvenient as degradation experiments often require significant amounts of time. The actual levels of degradation and temperature need to be measured at constant reference points at regular intervals, leading to complex setups. When the power architecture changes, these measurements would need to be repeated, further increasing the impracticability. Hence, it would be beneficial to use a Kalman filter similar to the approaches above, employing knowledge of the system to eliminate the need for vast amounts of training data. However, the system model itself is changing due to degradation, causing deviations in R_{th}. Several combined state and model parameter estimation methods exist. Extended Kalman filter (EKF) based methods are popular as they incorporate the advantages of controlled noise filtering of a Kalman filter, while able to deal with the non-linearity, introduced by considering model parameters as variables. The most common methods are generic joint estimation and generic dual estimation. In generic joint estimation, the state vector and parameters are combined in a new augmented state vector and the EKF simultaneously estimates the parameters and the state. This, however, leads to large matrix operations and to a potentially poor conditioned

numeric problem, as the parameters and state vary at a significantly different time scale. Hence, in this work, generic dual estimation or a Dual Extended Kalman Filter (DEKF) algorithm will be used. The first filter is used to estimate the junction temperature T_{die} based on the thermal model and the second filter is used to update the thermal model parameters. As indicated in Table I, this allows to achieve a highly accurate die temperature profile, together with a precise estimate of the time evolution of the reference values $R_{DS\ (on)}$ and R_{th}, indicating the damage magnitude and location. There is no need for training data and re-calibration of the filter. The main disadvantage is the need for a thermal model of the component, but, it will be shown that this model can be easily acquired. The computational resources used, will be slightly larger compared to the single EKF methodologies presented in literature, however, the difference will be limited as the state vectors can be kept small. In terms of required resources, going from one to two measurements raises the amount of required components. As can be seen, some of the other methodologies use similar component counts, however, this are mostly measurements which are already present for control purposes (shown with brackets). For the presented methodology, the final cost could be kept small as the measurement circuits could be easily integrated into the gate driver. Notwithstanding, currently, discrete components are used. This paper will demonstrate this methodology for a MOSFET in a solar photovoltaic (PV) boost converter which was purposely built. The test is done under the application of a realistic highly varying irradiance input profile while executing a Maximum Power Point Tracking (MPPT) algorithm. This shows that the methodology works under complex input profiles and control schemes.

3) Paper structure: The paper is organized as follows: First, the Kalman filter methodology is explained together with the thermal model in Section II. Next, the experimental setup together with the implementation of the measurement circuits, is shown in Section III. After this, the results of both a simulation and physical lab-experiment are discussed in Section IV. Finally, the paper is concluded in Section V.

II. Degradation Detection Methodology

A. Overview of the methodology

The aim of this work is to estimate the time evolution of the reference values $R_{DS\ (on)}$ and R_{th} as these reflect bond wire and solder layer degradation in the MOSFET. The $R_{DS\ (on)}$ can be directly measured and could, in principle, be directly compensated for temperature variations, estimated via a R_{gate} measurement. Unfortunately, this gives no information about the R_{th} evolution and lots of noise remains present in the measurement. Filtering noise on the R_{gate} based temperature estimate T_{die}, can be done with a first Kalman filter, using the thermal model of the device. The thermal model itself is also subjected to change as R_{th} degrades as well. Hence, not only the state variables (T_{die}) but also the model parameters (R_{th} and $R_{DS\ (on)}$) need to be estimated by a second Kalman filter.

B. Dual Extended Kalman filter algorithm

A Kalman filter is an algorithm that estimates unknown state variables x_k, given a set of noisy measurements y_k over time. When the system state space model is linear, as given in (1) and (2), a basic Kalman filter algorithm can be used. The state vector x_k is

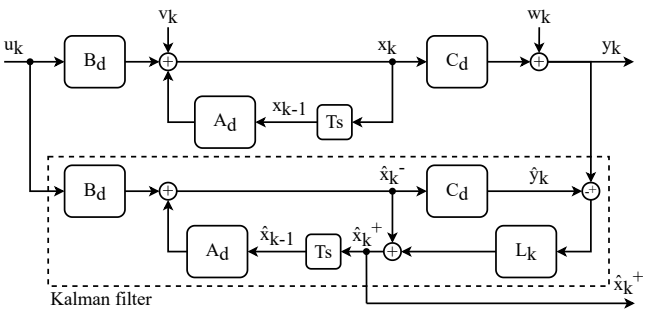

Fig. 2: Schematic overview of the plant and the discrete Kalman filter algorithm.

dependent on the previous state x_{k-1} together with the previous system input vector u_{k-1}. The output measurement vector y_k is only dependent on the current state vector x_k. The subscript d denotes that the model is discrete, $w_k \sim \mathcal{N}(0,Q)$ and $v_k \sim \mathcal{N}(0,R)$ are the process and measurement noise vectors which are assumed to be Gaussian with zero mean and covariance Q and R.

$$x_k = A_d x_{k-1} + B_d u_{k-1} + w_{k-1} \tag{1}$$
$$y_k = C_d x_k + v_k \tag{2}$$

A schematic representation of the system together with an implemented Kalman filter is given in Figure 2. A Kalman filter operates in two steps. In the prediction step, the state space model is used to make an *a priori* estimate of the state $\hat{x}_k^-$ as given in (3). This state estimate can be used to estimate the measurement output $\hat{y}_k$ as seen in (5). This estimated output will differ from the actually measured output due to process and measurement noise, leading to the residual $\tilde{y}_k$ in (6). In the update step, $\tilde{y}_k$ is used to make a corrected *a posteriori* state estimate $\hat{x}_k^+$ in (8). The weight of the corrective term is determined by the estimator gain L_k. In a Kalman filter, this gain is chosen as such to minimise the covariance P_k of the residual $\tilde{y}_k$ as given in (7). The covariance is re-estimated in every step. A detailed derivation of the Kalman gain can be found in [24].

Predict step:

$$\hat{x}_k^- = A_d \hat{x}_{k-1}^+ + B_d u_{k-1} \tag{3}$$
$$P_k^- = A_d P_{k-1}^+ A^T + Q \tag{4}$$
$$\hat{y}_k = C_d \hat{x}_k^- \tag{5}$$

Update step:

$$\tilde{y}_k = y_k - \hat{y}_k \tag{6}$$
$$L_k = P_k^- C^T (R - C P_k^- C^T)^{-1} \tag{7}$$
$$\hat{x}_k^+ = \hat{x}_k^- + L_k \tilde{y}_k \tag{8}$$
$$P_k^+ = (I - L_k C) P_k^- \tag{9}$$

In conclusion, following this algorithm, the most likely state and output is estimated taking into account the noise on the measurement and in the plant.

When the system model is non-linear as given in equations 10 and 11, the EKF algorithm can be employed [25]. The state x_k and

measurement output y_k are expressed as non-linear functions of the state x_k and input u_k.

$$x_k = f(x_{k-1}, u_{k-1}) + w_{k-1} \tag{10}$$
$$y_k = h(x_k) + v_k \tag{11}$$

This algorithm is identical to the one above, with the addition of a linearisation step to achieve linear state space A_l and C_l matrices, in order to calculate the gain L_k and error covariance P_k. This is achieved by evaluating the Jacobian matrix in the operation point at each time step as given in (12) and (13) [25].

$$A_{dl\ k-1} = \left.\frac{\partial f}{\partial x}\right|_{\hat{x}^+_{k-1}, u_{k-1}} \tag{12}$$
$$C_{dl\ k} = \left.\frac{\partial h}{\partial x}\right|_{\hat{x}^-_k} \tag{13}$$

When not only the state needs to be estimated and the system parameters change over time as well, a DEKF can be employed. Here the state is estimated in a system model and the parameters are estimated in a parameter model. The system model of the DEKF is similar to an EKF. The main difference is the inclusion of time varying parameters θ_k in the state transition and measurement function as seen in (14) and (15) respectively. The used DEKF methodology is based on [26], where it is demonstrated for the control of autonomous vehicles. Vector θ_k contains the model parameters which are subjected to change, these are seen as additional inputs to the state model.

System model:

$$x_k = f(x_{k-1}, u_{k-1}, \theta_{k-1}) + w_{k-1} \tag{14}$$
$$y_k = h(x_k, \theta_k) + v_k \tag{15}$$

A state transition function for the parameters is defined in (16). As the parameters vary very slowly in time, they are modeled to remain constant with the addition of noise $r \sim \mathcal{N}(0, S)$. The parameter measurement function in (17) is again dependent on both θ_k and x_k, however, θ_k is the state vector of the parameter model while x_k is seen as an additional input. The noise on the parameter measurement output is $e \sim \mathcal{N}(0, T)$.

Parameter model:

$$\theta_k = \theta_{k-1} + r_{k-1} \tag{16}$$
$$d_k = g(\theta_k, x_k) + e_k \tag{17}$$

In conclusion, as the measurement functions of both the system model and parameter model depend on x_k and θ_k, they will need to pass on each others states as inputs.

These models can be linearized as shown below. It is assumed that the noise variances are constant in time and have a zero mean. This linearization step will be used to bring the models to a state space representation. The superscript indicates whether it is the system x or the parameter model θ.

$$A^x_{dl\ k} = \left.\frac{\partial f}{\partial x}\right|_{\hat{x}^+_k, u_k, \hat{\theta}^-_k} \tag{18}$$
$$C^x_{dl\ k} = \left.\frac{\partial h}{\partial x}\right|_{\hat{x}^-_k, \hat{\theta}^-_k} \tag{19}$$
$$C^\theta_{dl\ k} = \left.\frac{\partial g}{\partial \theta}\right|_{\hat{x}^-_k, u_k, \hat{\theta}^-_k} \tag{20}$$

Using these linearized state space models, the Kalman filter algorithm can be implemented, consisting of two steps for both the state and parameter model. The first step is the predict step for the parameter model. A parameter state estimate $\hat{\theta}^-_k$ is made based on the previous estimate $\hat{\theta}^+_{k-1}$, together with a new error variance $P^{\theta\ -}_k$. Next, the predict step of the system model takes place. A state estimate $\hat{x}^-_k$ is predicted based on the previous state estimate $\hat{x}^+_{k-1}$, the input u_{k-1}, and the additional input which is the previously estimated $\hat{\theta}^-_k$. A new error covariance $P^{x\ -}_k$ is calculated as well. Finally, the update step for both the system and parameter model can be executed. The respective measurement functions are used to calculate residuals $\tilde{y}_k$ and $\tilde{d}_k$. Based on the Kalman gain, the state estimates can be updated to $\hat{x}^+_k$ and $\hat{\theta}^+_k$. The error variances are updated as well.

Predict step parameter model:

$$\hat{\theta}^-_k = \hat{\theta}^+_{k-1} \tag{21}$$
$$P^{\theta\ -}_k = P^{\theta\ +}_{k-1} + S \tag{22}$$

Predict step system model:

$$\hat{x}^-_k = f(\hat{x}^+_{k-1}, u_{k-1}, \hat{\theta}^-_k) \tag{23}$$
$$P^{x\ -}_k = A^x_{dl\ k-1} P^{x\ +}_{k-1} {A^x_{dl\ k-1}}^T + Q \tag{24}$$

Update step system model:

$$\tilde{y}_k = y_k - h(\hat{x}^-_k, \hat{\theta}^-_k) \tag{25}$$
$$L^x_k = P^{x\ -}_k {C^x_{dl\ k}}^T (R - C^x_{dl\ k} P^{x\ -}_k {C^x_{dl\ k}}^T)^{-1} \tag{26}$$
$$\hat{x}^+_k = \hat{x}^-_k + L^x_k \tilde{y}_k \tag{27}$$
$$P^{x\ +}_k = (I - L^x_k C^x_{dl\ k}) P^{x\ -}_k \tag{28}$$

Update step parameter model:

$$\tilde{d}_k = d_k - g(\hat{x}^-_k, u_k, \hat{\theta}^-_k) \tag{29}$$
$$L^\theta_k = P^{\theta\ -}_k {C^\theta_{dl\ k}}^T (T - C^\theta_{dl\ k} P^{\theta\ -}_k {C^\theta_{dl\ k}}^T)^{-1} \tag{30}$$
$$\hat{\theta}^+_k = \hat{\theta}^-_k + L^\theta_k \tilde{d}_k \tag{31}$$
$$P^{\theta\ +}_k = (I - L^\theta_k C^\theta_{dl\ k}) P^{\theta\ -}_k \tag{32}$$

C. Thermal Foster and Cauer network

A thermal model of the MOSFET under investigation is needed in order to construct the Kalman filter, calculating the die temperature T_{die} based on the device power loss P_{loss}. Often a resistor-capacitor network is used, simplifying the heat transfer problem to a one-dimensional energy flow with uniform temperature at the material interfaces. This model is sufficient when trying to estimate the average temperature of the die as done in this work. Fig. 3a gives a Cauer network representation of the thermal path between the MOSFET die and the ambient air [27]. The non-linear convective resistance R_{conv} between the heatsink outer surface and the ambient air makes it difficult to describe this network in a state space representation. R_{conv} is dependent on the surface temperature T_{sink} which is a state variable. A function could be fitted to this dependency, after which the state space can be linearized around the current operation region of the MOSFET. However, for the sake of simplicity, in this analysis, the sink temperature T_{sink} is considered as a known value as it is easily accessible. When it is assumed that the sink temperature varies sufficiently slow, it can be considered as a constant offset to the die temperature T_{die}, allowing to simplify the thermal network to Fig. 3b.

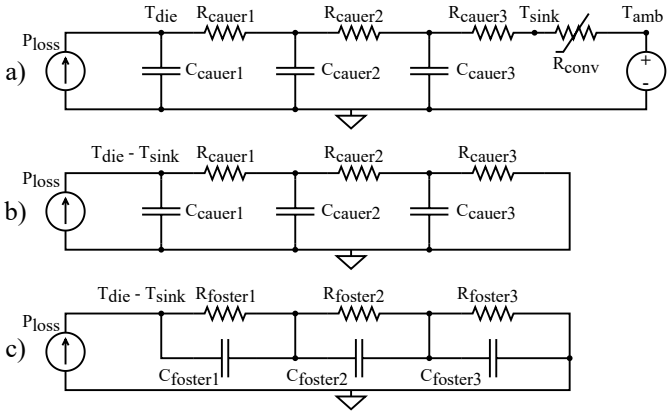

Fig. 3: Thermal network representation of a MOSFET with heatsink in Cauer and Foster configurations.

The equivalent Foster representation given in Fig. 3c, is also used as it is more suited for model estimation via characterization tests. The temperatures in between the different cells do no longer represent physical temperatures. Estimation is done by measuring the transient thermal impedance $Z_{th}(t)$ of the system and fitting the expression for the time dependent thermal impedance of the Foster network to it. The expression is given in (33) and is a sum of exponential terms corresponding to the different cells of the Foster network [28].

$$Z_{th}(t) = \sum_{i=1}^{n} R_i \left(1 - e^{\frac{-t}{R_i C_i}}\right) \tag{33}$$

The thermal resistance R_{th} degradation mostly occurs at the die. Unfortunately, in a Foster network, the physical meaning of the resistances is lost. This makes it impossible to assign the degradation to one particular resistance. Hence, after estimation the Foster network needs to be transformed back to its physical Cauer representation. The resulting thermal layers do not correspond exactly with the actual physical component layers as this would require the heat to travel uniformly in only one direction. Fortunately, this is often a reasonable approximation, making it possible to assign degradation to the front part of the thermal path, corresponding to its physical location (solder layer).

The Cauer network can be written in the state space representation as shown in (34) and (35) [13]. In this study a third order model will be used. The subscript c denotes that this is a continuous time model. The Kalman filter algorithm used in this work requires a discrete state space formulation. Several discretization methods exist in literature, in this work the backward Euler method will be used as given in (36)-(40). T_s represents the sampling time.

$$\begin{bmatrix} \dot{T}_1 \\ \dot{T}_2 \\ \dot{T}_3 \end{bmatrix} = \begin{bmatrix} -\frac{1}{R_1 C_1} & \frac{1}{R_1 C_1} & 0 \\ \frac{1}{R_1 C_2} & -\frac{1}{R_1 C_2} - \frac{1}{R_2 C_2} & \frac{1}{R_2 C_2} \\ 0 & \frac{1}{R_2 C_3} & -\frac{1}{R_2 C_3} - \frac{1}{R_3 C_3} \end{bmatrix} \begin{bmatrix} T_1 \\ T_2 \\ T_3 \end{bmatrix} + \begin{bmatrix} \frac{1}{C_1} \\ 0 \\ 0 \end{bmatrix} P_{loss} \tag{34}$$

$$T_{jc} = T_{die} - T_{sink} = \begin{bmatrix} 1 & 0 & 0 \end{bmatrix} \begin{bmatrix} T_1 \\ T_2 \\ T_3 \end{bmatrix} \tag{35}$$

$$x(t+T_s) = x(t) + T_s f(x(t+T_s), u(t+T_s)) \tag{36}$$

$$A_d = (I - T_s A_c)^{-1} \tag{37}$$

$$B_d = (I - T_s A_c)^{-1} T_s B_c \tag{38}$$

$$C_d = C_c \tag{39}$$

$$D_d = D_c \tag{40}$$

D. Dual Extended Kalman filter condition monitoring

The first system Kalman filter uses the thermal model to estimate the die temperature T_{jc} (T_{die} relative to T_{sink}) based on the power loss P_{loss}. In the MOSFET, both the parameters $R_{DS(on)}$ and R_{th} are subjected to change, however, only the R_{th} is part of the thermal model state space. Although $R_{DS(on)}$ has no direct link with the first Kalman filter, it can still be added to the second parameter estimation Kalman filter. This way, the indirect dependence of $R_{DS(on)}$ on R_{th} through temperature can be taken into account.

This leads to the following state selection x for the system model (first Kalman filter). The first variable is the die temperature T_{jc} while the others represent the relative temperatures of the layers within the Cauer network.

$$\begin{bmatrix} x_1 \\ x_2 \\ x_3 \end{bmatrix} = \begin{bmatrix} T_{die} - T_{sink} \\ T_2 \\ T_3 \end{bmatrix} \tag{41}$$

The measurement output of the state model y will be T_{jc} to allow for comparison with the measured temperature through the R_{gate} measurement in the update step. The input u will be P_{loss}.

$$y = T_{die} - T_{sink} \tag{42}$$

$$u = P_{loss} \tag{43}$$

For the parameter model states θ (second Kalman filter), the two varying parameters $R_{DS(on)}$ and R_{th} are selected. Note that the $R_{DS(on)}$ is explicitly converted to a reference temperature T_{ref} and thus only changes due to degradation.

$$\begin{bmatrix} \theta_1 \\ \theta_2 \end{bmatrix} = \begin{bmatrix} R_{th} \\ R_{DS(on)}(T_{ref}) \end{bmatrix} \tag{44}$$

As output d, T_{jc} is selected together with $R_{DS(on)}$ which is now the actual temperature dependent parameter. These will again be compared with the measured temperature through the R_{gate} measurement and the measured $R_{DS(on)}$ during the update step. In order to allow the translation of $R_{DS(on)}(T_{ref})$ to $R_{DS(on)}(T_{die})$, an additional input $n = T_{sink}$ is used. This allows to use the absolute T_{die} in the temperature correction instead of the relative T_{jc}.

$$\begin{bmatrix} d_1 \\ d_2 \end{bmatrix} = \begin{bmatrix} T_{die} - T_{sink} \\ R_{DS(on)}(T_{die}) \end{bmatrix} \tag{45}$$

$$n = T_{sink} \tag{46}$$

The state space matrices can now be adapted to include the varying parameter R_{th}. The assumption is made that the thermal path mostly degrades close to the die which translates in the increase of thermal resistance R_1. The additional input variable $\gamma = R_1 = R_{th}$ allows to change this parameter in the A matrix. Note that these matrices are

still continuous and need to be discretized using the Euler algorithm. The subscript c becomes subscript d after discretization.

$$A_c^x(\gamma)=\begin{bmatrix} -\frac{1}{\gamma C_1} & \frac{1}{\gamma C_1} & 0 \\ \frac{1}{\gamma C_2} & -\frac{1}{\gamma C_2}-\frac{1}{R_2C_2} & \frac{1}{R_2C_2} \\ 0 & \frac{1}{R_2C_3} & -\frac{1}{R_2C_3}-\frac{1}{R_3C_3} \end{bmatrix} \quad (47)$$

$$B_c^x=\begin{bmatrix} \frac{1}{C_1} \\ 0 \\ 0 \end{bmatrix} \quad (48)$$

$$C_c^x=\begin{bmatrix} 1 & 0 & 0 \end{bmatrix} \quad (49)$$

Using the discrete versions of these matrices, it is possible to define the state transition function f and the measurement functions h for the system model which can be used in first Kalman filter. Note that these matrices are still non-linear.

$$x_{k+1}=f(x_k,u_k,\theta_k)=A_d^x(\theta_{k1})x_k+B_d^x\,u_k \quad (50)$$

$$y_k=h(x_k)=C_d^x\,x_k \quad (51)$$

Defining the measurement function of the parameter model g is more complicated. d_1 represents T_{jc} and should be linked to θ_{k1} which represents the thermal resistance R_{th}. This can be with the same equations (50) and (51), using x_{k-1} as an input and θ_{k1} as state variable. d_2 represents the temperature dependent $R_{DS(on)}(T_{die})$ while θ_{k2} represent the same resistance at reference temperature $R_{DS(on)}(T_{ref})$. The thermal dependence can be modeled with (52), α is a fitting parameter [29].

$$R_{DS(on)}(T_{die})=R_{DS(on)}(T_{ref})\cdot\left(1+\frac{\alpha}{100}\right)^{T_{die}-T_{ref}} \quad (52)$$

The temperature T in this expression equals the die temperature which is equal to d_1 summed with the sink temperature in the additional input n. This leads to the final expression for g in (53).

$$d_k=g(h(f(x_{k-1},u_{k-1},\theta_k)),\theta_k,n_k)= \begin{bmatrix} C_d^x\,(A_d^x(\theta_{k1})x_{k-1}+B_d^x\,u_{k-1}) \\ \theta_{k2}\,(1+\frac{\alpha}{100})^{d_{k1}+n_k-T_{ref}} \end{bmatrix} \quad (53)$$

The state transition function f and the measurement functions h and g can be used to calculate the matrices A_{dl}^x, C_{dl}^x and A_{dl}^θ by taking the jacobian as given in (18), (19) and (20). This only needs to happen once after which the analytical expression can be used in the DEKF algorithm. Fig. 4a gives a graphical representation of the final algorithm. The detailed functioning of the two Kalman filters is presented in Fig. 4b.

It is important to note that (52) only takes the temperature dependence of $R_{DS(on)}$ into account. Generally $R_{DS(on)}$ is also dependent on the drain to source current I_{DS}. Often, this dependency is quite limited at the recommended gate voltage in the mayor part of the operating range. When this is not the case, (52) should be extended to also incorporate this current dependence. In principle, this is not a problem as this current is already measured. However, in this work, the current dependency is omitted.

III. Experimental validation setup

In this section the design of the experimental validation setup is discussed. First, the used converter and the implemented measurement circuits will be explained. Second, the circuits are characterized, determining the temperature dependence of the different measurements together with the confidence interval around these measurements.

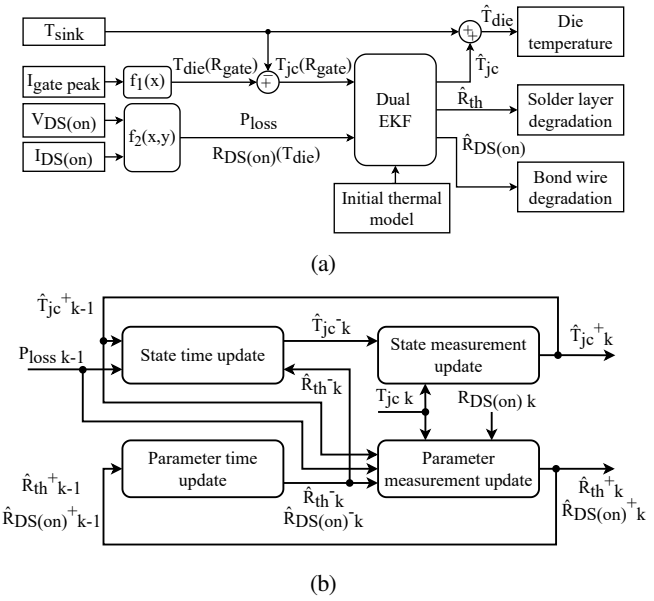

Fig. 4: Schematic representation of the DEKF algorithm used to estimate T_{die}, $R_{DS(on)}$ and R_{th}: (a) System overview and, (b) detailed representation of the DEKF algoritm.

TABLE II: Summary of the most important characteristics of Infinion MOSFET IPP600N25N3.

Parameter	Symbol	Value	Unit
Maximum drain to source voltage	$V_{DS\ max}$	250	V
Maximum drain to source resistance	$R_{DS\ max}$	60	$m\Omega$
Maximum drain to source current	$I_{D\ max}$	25	A
Thermal resistance	R_{thJC}	1.1	K/W
Internal gate resistance	$I_{G\ internal}$	2.5	Ω
Rise time	t_r	10	ns
Fall time	t_f	8	ns

A. Converter topology and measurements

A PV use-case was selected as it is characterized by highly varying mission profiles and changing operation set-points due to MPPT. A schematic representation of the boost converter together with the implemented measurements is shown in Fig. 5a. As Device Under Test (DUT) MOSFET IPP600N25N3 with a TO220 package was selected. The most prominent characteristics of the MOSFET are summarized in Table II. $R_{DS(on)}$ will be determined by measuring the drain to source on-state voltage $V_{DS(on)}$ and current $I_{DS(on)}$, R_{gate} will be determined by measuring the peak current to the gate during turn-on $I_{gate\ peak}$. The input power measurement is needed for the execution of MPPT. A picture of the complete PCB is given in Fig. 5b.

1) $V_{DS\ (on)}$ measurement circuit: During the on-state of the component, an accurate measurement of the voltage needs to be taken, while the sensor is exposed to the full bus voltage when the MOSFET turns off. The sensitivity of the voltage drop to temperature is in the order of 2 $mV/°C$ at 4A. There are no sensors with the required accuracy that can withstand this voltage range. Hence, a clipping circuit is needed. In this work, the circuit presented in [30] will be used, a simplified schematic is given in Fig. 6a. Other circuits can be used as well, some examples tested in literature can be found in [31]–[33].

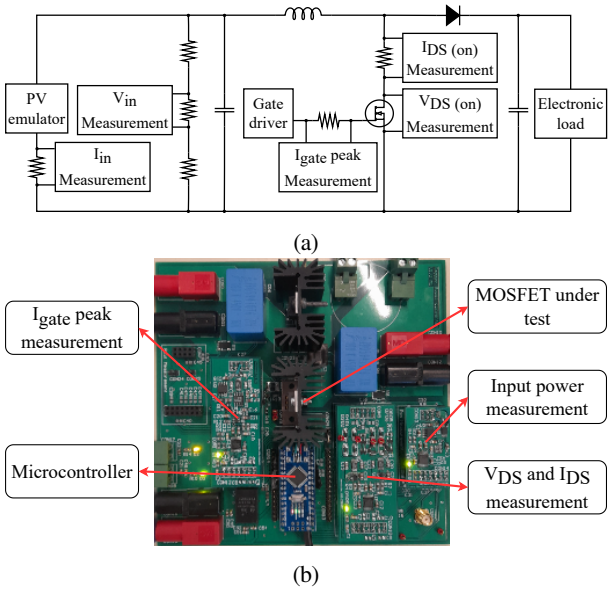

Fig. 5: Experimental setup: (a) Schematic representation of the boost converter with location of the control and condition monitoring measurements; (b) Picture of the boost converter board with indication of the different condition monitoring measurement circuits.

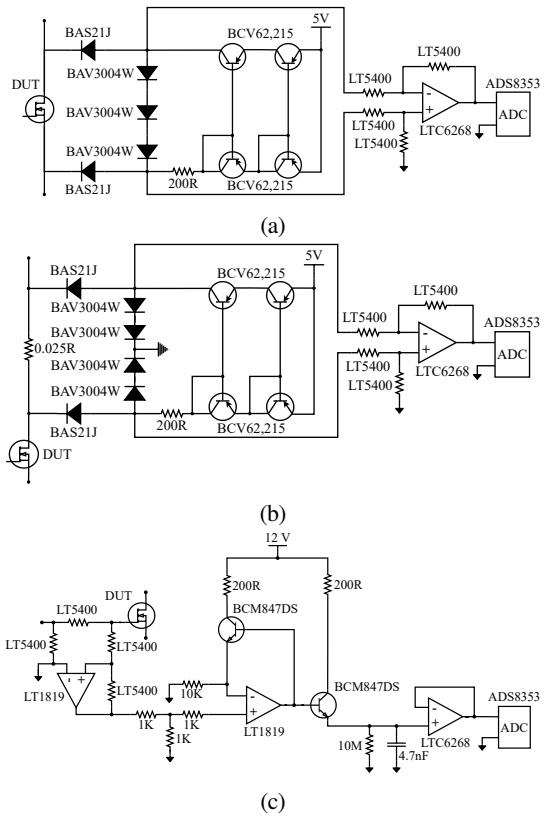

Fig. 6: Temperature and damage sensitive parameter measurement circuits: (a) Vds(on) measurement circuit, (b) Ids(on) measurement circuit and, (c) Igate peak measurement circuit.

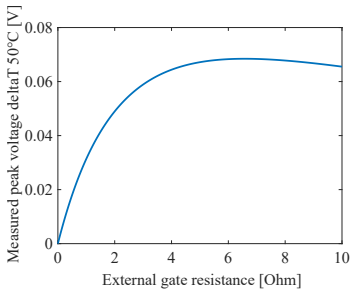

Fig. 7: Measured voltage peak versus the external gate resistance.

2) $I_{DS(on)}$ measurement circuit: The $I_{DS(on)}$ measurement circuit will be implemented using a shunt resistor in order to allow for a current measurement with sufficient bandwidth. The shunt resistor is placed at the drain side of the MOSFET to avoid interference with the R_{gate} measurement. The drain side experiences high voltages when the MOSFET is in the blocking state. This can be solved in a similar way as was done for the $V_{DS(on)}$ measurement, with a clipping circuit. The modified version of the clipping circuit is given in Fig. 6b.

3) R_{gate} measurement circuit: Measuring the internal gate resistor R_{gate} can be done by detecting the magnitude of the peak current $I_{gate\ peak}$ going to the gate [33]–[35]. The sensitivity of the internal gate resistance to temperature is in the order of $\phi = 0.6\ m\Omega/°C$. As $I_{gate\ peak}$ occurs in a very short time frame, most ADCs are not capable to sample the peak value. Hence, a peak detection circuit is used [33]. The final circuit is given in Fig. 6c. The magnitude of $I_{gate\ peak}$ and the measured voltage $V_{measure}$ over the external gate resistance $R_{gate\ ext}$ used as a measurement shunt, can be expressed by (54) and (55). $R_{gate}(T_{ref})$ is the internal gate resistance at reference temperature T_{ref}, the voltage applied by the transistor driver is given by V_{driver}. Equation (55) implies that an optimal resistance $R_{gate\ ext}$ can be chosen as adding resistance decreases the sensitivity of the current $I_{gate\ peak}$ to temperature T_{die}, but increases the measured voltage $V_{measure}$ for a certain $I_{gate\ peak}$.

$$I_{gate\ peak} = \frac{V_{driver}}{R_{gate\ ext} + R_{gate}(T_{die})} \tag{54}$$

$$V_{measure} = \frac{V_{driver}\ R_{gate\ ext}}{R_{gate\ ext} + R_{gate}(T_{ref}) + \phi\ (T_{die} - T_{ref})} \tag{55}$$

Fig. 7 shows the magnitude of the measured voltage for a temperature difference of 50 $°C$ in function of the external gate resistance. It can be seen that $R_{gate\ ext} = 6\ \Omega$ is ideal for this specific use-case, however, the optimum is dependent on the temperature difference observed. As the curve decreases very gradually after the optimum, in this work $R_{gate\ ext} = 10\ \Omega$ is chosen to provide a satisfactory performance over the entire range.

B. Parameter temperature dependence and measurement circuit validation

In order to use the $R_{DS\ (on)}$ and R_{gate} measurement circuits to sense the die temperature, the temperature dependence of these parameters needs to be known. This will be done based on an independent reference measurement of the $R_{DS\ (on)}$ temperature dependence, which can then be used to calibrate the $R_{DS\ (on)}$ and R_{gate} measurement circuits and express their measurement uncertainty.

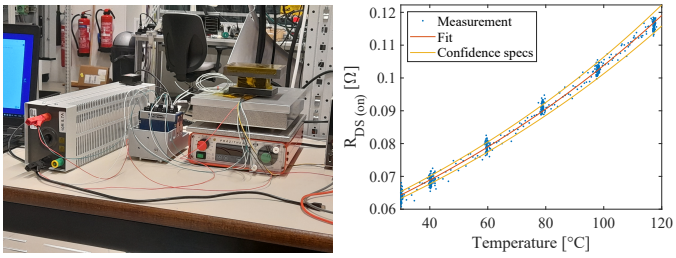

(a) (b)

Fig. 8: Determination of the $R_{DS\ (on)}$ temperature dependence: (a) The $R_{DS\ (on)}$ temperature dependence measurement setup; (b) The reference temperature dependence fitted on measurements taken with K-type thermocouple XE-3505-001, and NI9213/NI9229 data acquisition boxes together with the 95 % confidence interval.

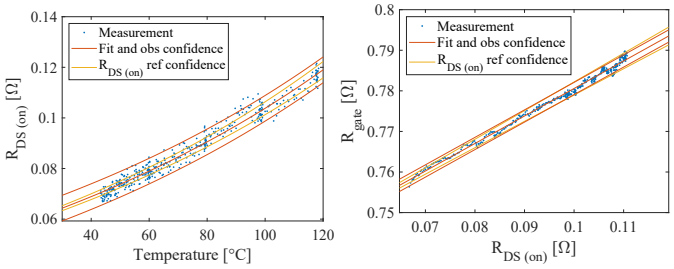

(a) (b)

Fig. 9: Determination of the temperature dependence of the parameter measurement: (a) Measurement circuit $R_{DS\ (on)}$ values in function of hotplate temperature, temperature dependence fit and 95 % observational confidence interval, and the 95 % confidence interval of the $R_{DS\ (on)}$ reference temperature dependency; (b) Simultaneous measurement of the $R_{DS\ (on)}$ and R_{gate} during converter operation, the linear fit between the two and the previously observed 95 % observational confidence interval, and the 95 % confidence interval of the $R_{DS\ (on)}$ reference temperature dependency.

1) Reference $R_{DS\ (on)}$ temperature dependence: The reference $R_{DS\ (on)}$ temperature dependence can be extracted by pressing the MOSFET onto a hotplate. The temperature is increased in steps allowing the device to reach thermal equilibrium at the end of every step. A small sense current of 0.05A is applied which can be translated into $R_{DS\ (on)}$ by measuring V_{DS}. The gate is constantly at 12 V to ensure that the device is always turned on and the measurement current is sufficiently small to avoid device self heating, allowing to assume a uniform temperature inside the device. A picture of the characterization setup is given in Fig. 8a. The hotplate can be seen, the temperature is measured with K-type thermocouple XE-3505-001 and a NI9213 data acquisition box (DAQ). A resistor is placed in series with the sense current source to fine-tune the measurements. A NI9229 DAQ is used to sense both the measurement current and voltage. The resulting temperature dependent $R_{DS\ (on)}$ measurements can be seen in Fig. 8b. The temperature dependence is fitted through the measurement points and the 95 % confidence interval is indicated. It is determined based on the specifications of the used measurement devices (resistance and temperature), and the uncertainty on the fit itself (which is small due to the high number of measurement points). The average uncertainty on the $R_{DS\ (on)}$ measurement is $\pm 1.9\ m\Omega$, which corresponds to an uncertainty in the temperature dependence of $\pm 3.09\ °C$.

2) $R_{DS\ (on)}$ measurement temperature dependence: A similar experiment can be done, however, now the custom designed $R_{DS\ (on)}$ measurement board will be used. The resulting measurement points can be seen in Fig. 9a together with the 95 % observational confidence interval which encompasses an expected 95 % of new measurements. The average confidence on a single $R_{DS\ (on)}$ measurement is $\pm 5.1\ m\Omega$, which corresponds to $\pm 8.61\ °C$. Luckily multiple measurements can be used to fit the actual temperature dependence based on the measurements resulting in a confidence of the fit of $\pm 0.35\ m\Omega$, which corresponds to $\pm 0.59\ °C$. As these measurements are tuned based on the previous reference measurement, the uncertainties can be propagated to result in a uncertainty of $\pm 2.0\ m\Omega$, which corresponds to $\pm 3.15\ °C$ on the temperature dependence trend produced by the $R_{DS\ (on)}$ measurement board.

3) R_{gate} measurement temperature dependence: The temperature dependence of R_{gate} measured using the custom measurement board cannot be measured using the same procedure above as R_{gate} can only be measured in switching operation. This will cause additional losses resulting and the assumption of limited self heating no longer being valid. Luckily, the $R_{DS\ (on)}$ can be measured simultaneously with R_{gate}, allowing to establish a link between these two parameters and indirectly between R_{gate} and temperature. The resulting simultaneous measurement of R_{gate} and $R_{DS\ (on)}$ during operation can be seen in Fig. 9b. A linear relation can be fitted. The observational uncertainty of the R_{gate} measurement is $\pm 1.5\ m\Omega$, corresponding to $\pm 3.78\ °C$ which is in the same range as the uncertainty of the $R_{DS\ (on)}$ reference. Again, due to repeated measurements, the uncertainty on the fit itself can be reduced to only $\pm 0.123\ m\Omega$. Taking into account the uncertainty on the temperature measurement using $R_{DS\ (on)}$, a final uncertainty of $\pm 3.18\ °C$ is found for the resulting temperature dependence of R_{gate} measured by the custom board.

C. Thermal model characterization

In order to implement the DEKF, the thermal model needs to be known. A power step is used to perform the thermal transient measurement [36]. The current through $R_{DS\ (on)}$ is both used for measurement and heating of the device. A feedback loop is implemented to ensure the power dissipation remains constant at 9 W despite the increase of $R_{DS\ (on)}$ with temperature. The measured sink temperature and die temperature are shown in Figure 10a. Based on these measurements, the transient impedance curve can be calculated. Using a least square algorithm, the Foster network impedance was fitted as can be seen in Figure 10b. Afterwards, this can be converted to a Cauer network representation. In this work, a model of degree three is used which proved to be optimal. Increasing the degree of the model further, resulted in very small time constant of the additional layer, falling outside of the observable range with the used sampling frequency of 5 Hz. Hence, the additional layer is not contributing to an increased accuracy of the response. To test the performance of the resulting thermal model, the modeled step response is compared to the measured data in Figure 10c. It can be seen that the difference is always within 1 degree.

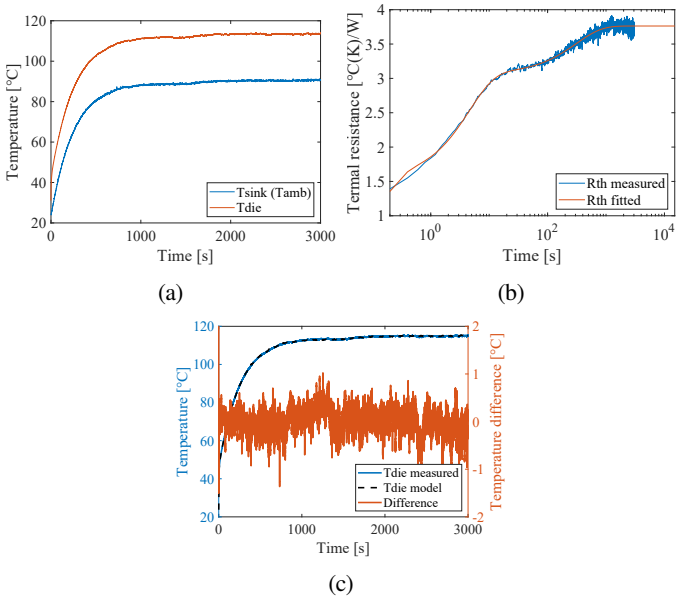

Fig. 10: Example of a thermal Foster network estimation test. (a) Measured heat sink and MOSFET die temperature as response to a constant power dissipation step. (b) Measured thermal impedance transient and fitted Foster network thermal transient. (c) Measured and simulated step response using the estimated Foster network and the respective difference.

TABLE III: Parameters of the boost converter, measured signal variances and results of the thermal characterization experiments.

Converter parameters		Characterization results	
Parameter	Value	Parameter	Value
$V_{in\ max}$	40 V	$Var(T_{die})$	7.8880 K
V_{out}	100 V	$Var(R_{DS(on)})$	0.1118 $\mu\Omega$
P_{max}	300 W	$Var(State\ plant)$	100 nK
C_{input}	10 μF	$Var(Parameter\ plant)$	0.01 $n\Omega$
C_{output}	10 μF	$R_{ref\ R_{DS(on)}}$	0.06246 Ω
L	200 μH	$\alpha_{R_{DS(on)}}$	0.70818 Ω/K
f_{sw}	50 kHz	$R_{ref\ R_{gate}}$	0.71269 Ω
$R_{turn-on}$	10 Ω	$\alpha_{R_{gate}}$	0.17270 Ω/K
$R_{turn-off}$	5 Ω	R_1	2.2117 K/W
		R_2	1.4691 K/W
		R_3	0.30939 K/W
		C_1	0.053088 J/K
		C_2	2.8877 J/K
		C_3	1136.8 J/K

D. Experimental setup summary

The final boost converter parameters, the results of the thermal dependence characterization and the thermal model fit are summarized in Table III. The variances of the measurement signal are given as well as they are needed to tune the Kalman filter. Constant value reference measurement are taken to characterize this noise variance. The values found are different from the uncertainty intervals on the measurement given above, as only the contribution of noise is taken into account and not the offset and scale errors because the filter can only remove Gaussian noise. The plant variances are chosen by minimizing the root mean square estimation error in simulation.

IV. Experimental results and discussion

The aim of this section is to demonstrate and verify the capabilities of the proposed methodology. $R_{DS(on)}$ and R_{gate} measurements, processed by the DEKF, should be to estimate the die temperature and amount of damage, and distinguish between failure modes. The simulation study allows to insert precise amounts of degradation and controlled levels of noise into the simulated measurement signals. This way, it will be possible to evaluate whether the filter can extract the known degradation in the signal under the presence of noise, validating the mathematical methodology. Second, the resilience against errors in the temperature dependence of the parameters will be tested and quantified. After this, the experimental setup will be used to show that the proposed measurements, with their confidence intervals, allow to reliably filter the R_{gate} based temperature measurement, and estimate the degradation in $R_{DS(on)}$ and R_{th}. The Kalman filter residual and fixed condition $R_{DS(on)}$ measurements will be used to check whether the filter output is able to remain within the confidence intervals of the input signals.

A. Simulation results

In this section, the DEKF is tested on artificial data. The thermal characterization measurements were used to construct a virtual model, implementing the actual measured resistance-temperature characteristics and Cauer model, allowing to translate an irradiance profile into simulated $R_{DS(on)}$ and R_{gate} measurements. The data generation algorithm starts with determining the duty cycle based on the input voltage, current and duty cycle in the previous time-step, using a perturb and observe MPPT algorithm. Using a PV model and electrical converter model, the new input voltage and current can be calculated, resulting from the adjusted duty cycle and the new irradiance value. Next, the $R_{DS(on)}$ and R_{gate}, based on T_{die} in the previous time-step and the power losses in the MOSFET can be calculated. Based on these power losses, the next die temperature can be calculated, using the discrete thermal state space model. Depending on the frequency of the MPPT, the cycle is repeated by calculating a new duty cycle or the present value is reused to calculate a new input voltage and current. Exponential degradation is introduced using (56) and (57), β_1 and β_2 are used to set the degradation rate. Additive Gaussian noise is added to the measurement signals with the variances equal to these measured in the lab setup.

$$R_{DS(on)\ k+1} = R_{DS(on)\ 1}(T_{die\ k})\ e^{\beta_1 T_s k} \tag{56}$$

$$R_{th\ k+1} = R_{th\ k}(1+\beta_2 T_s) \tag{57}$$

1) Estimation results: Fig. 11a shows the used irradiance profile and Fig. 11b the synthetically generated $R_{DS(on)}$ and R_{gate} resistance measurements. Fig. 11c shows the die temperature T_{die} estimated by the Kalman filter. This T_{die} is used to convert the temperature dependent $R_{DS(on)}$ to a fixed reference temperature $T_{ref} = 25\ °C$, allowing to see the evolution of the degradation. In Fig. 11d, this temperature compensated $R_{DS(on)}$ resistance and the R_{th} resistance are given. A random initial estimate of these parameters was used but the filter quickly converges to the correct values due to adequate tuning. The RMSE between the Kalman filter estimate and the actual $R_{DS(on)}$ and R_{th} trajectory is 9.9719 $\mu\Omega$ and 1.9 mW/K respectively. This nearly perfect estimation is expected as the noise is perfectly Gaussian with known covariance. The temperature dependence of $R_{DS(on)}$ and

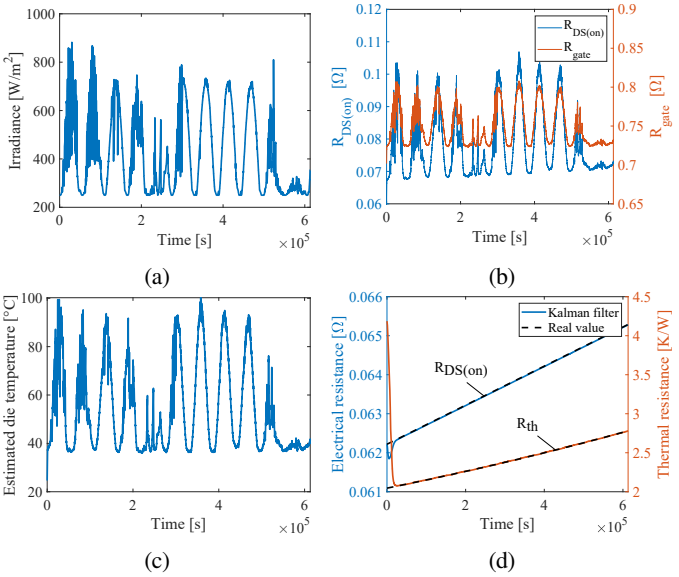

Fig. 11: Kalman filter test using synthetic data with Gaussian noise added to the simulated $R_{DS(on)}$ and $I_{gate\ peak}$ measurements: (a) Solar irradiance profile and, (b) simulated $R_{DS(on)}$ resistance and R_{gate} resistance; (c) Kalman filter estimation of the die temperature T_{die}; (d) Kalman filter estimation of $R_{DS(on)}$ resistance at reference temperature $T_{die} = 25\ °C$ and Kalman filter estimation of R_{th} resistance compared to the actual $R_{DS(on)}$ resistance at reference temperature $T_{die} = 25\ °C$ and actual R_{th} resistance present in the synthetic data.

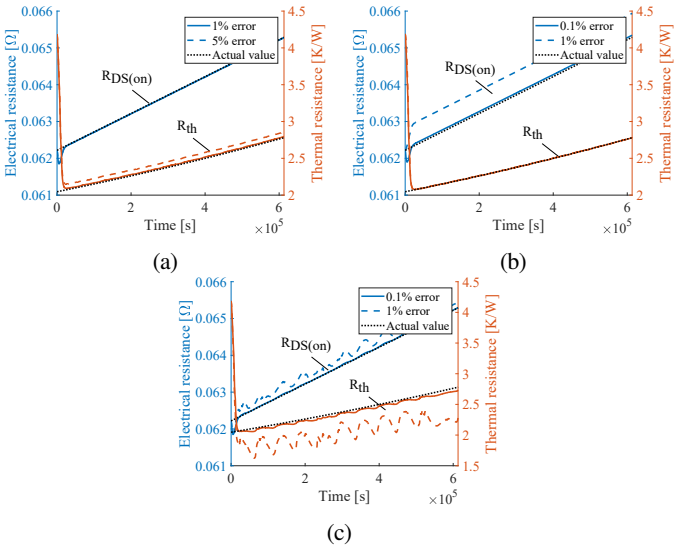

Fig. 12: Sensitivity analysis using synthetic data with Gaussian noise added to the simulated $R_{DS(on)}$ and $I_{gate\ peak}$ measurements with characterization errors: (a) Thermal capacitance and resistance estimation error, (b) $R_{DS(on)}$ temperature dependence estimation error and, (c) R_{gate} temperature dependence estimation error.

R_{gate} is also know perfectly as the same relationship was used to generate both the artificial data and implement the Kalman filter.

2) Sensitivity to characterization errors: In this section a sensitivity analysis is performed in order to investigate the importance of modeling and characterization errors for the performance of the DEKF. In Fig. 12a, the impact of a thermal modeling error is shown. Both the middle layer thermal resistance R_2 and capacitance C_2 were decreased with 1 and 5 percent respectively. The influence is only minor and causes a fixed overestimation of the die thermal resistance R_1, which is of no concern when aiming to detect degradation. In Fig. 12b, a 0.1 and 1 percent underestimation error to the conversion from die temperature T_{die} to $R_{DS(on)}$ is added. It can be seen that the influence is relatively larger due to the small degradation values compared to its magnitude. However, if the error is consistent over the range of $R_{DS(on)}$, this again leads to a constant offset error. Hence, this does hinder the ability to assess the damage over time. Lastly, Fig. 12c shows the influence of adding a 0.1 and 1 percent underestimation error on the conversion of R_{gate} to T_{die}. It can be seen that the impact is more problematic in this case as the thermal and electrical effects cannot be decoupled properly. The filter has difficulty assigning degradation to either $R_{DS(on)}$ and R_{th}, leading to oscillations in the result observed. Hence, R_{gate} needs to be characterized carefully. As previously determined, the 95 % confidence interval on R_{gate} is on average $\pm 1.3\ m\Omega$ ($\pm 0.8\ m\Omega - \pm 2.2\ m\Omega$ over the entire range of $30\ °C - 120\ °C$ corresponding to $\pm 0.10\ \% - \pm 0.28\ \%$). This indicates that the issue might occur to a lesser extend at the higher temperature range during the lab experiment. It is important to note that in this case the degradation can still be observed, however, the filter sometimes assigns degradation to the incorrect failure mode.

TABLE IV: Summary of the influence of characterization errors.

Misestimation location	Misestimation magnitude	Influenced parameter	Mean error	Error variance
Thermal model	1 %	$R_{DS(on)}$ [Ω]	9.8514e-06	2.2477e-12
		R_{th} [W/K]	-0.0160	4.1631e-06
	5 %	$R_{DS(on)}$ [Ω]	8.9381e-06	4.2612e-12
		R_{th} [W/K]	-0.0775	4.1165e-06
$T_{die}(R_{DS(on)})$	0.1 %	$R_{DS(on)}$ [Ω]	-5.3754e-05	3.6801e-12
		R_{th} [W/K]	-6.7887e-04	4.6239e-06
	1 %	$R_{DS(on)}$ [Ω]	-6.3411e-04	8.3496e-11
		R_{th} [W/K]	-8.1247e-04	4.7892e-06
$T_{die}(R_{gate})$	0.1 %	$R_{DS(on)}$ [Ω]	-1.1460e-05	5.8941e-11
		R_{th} [W/K]	0.0349	1.7842e-04
	1 %	$R_{DS(on)}$ [Ω]	-2.0477e-04	6.2345e-09
		R_{th} [W/K]	0.3515	0.0134

A summary of the errors in the predicted $R_{DS(on)}$ and R_{th}, due to these characterization errors, can be found in Table IV. The error mean is given as well as the error variance. The variance is the most important metric as constant offsets are acceptable for the purpose of condition monitoring.

B. Lab experiment results

The simulation study showed that the filter functions properly, however, errors in the temperature characteristics might influence the accuracy of the results. In this section, the result of the filter using the actual measurement circuits in a PV converter will be given. After an initial visual inspection of the results, the filter residual will be used to verify whether the filter is functioning within the noise range of the input signals. The resistance prediction results will also be compared to periodic measurements at fixed condition to verify the validity.

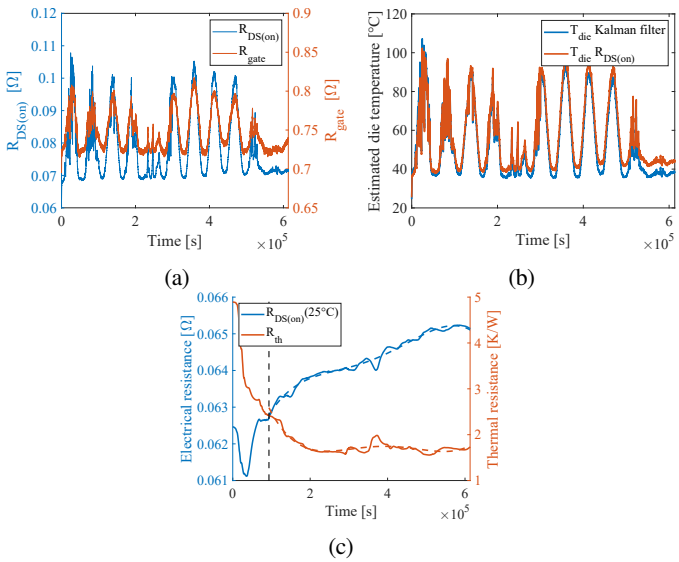

Fig. 13: Lab experiment with emulated PV panel and MPPT: (a) Measured $R_{DS(on)}$ resistance and R_{th} resistance; (b) Kalman filter estimation of T_{die} together with an estimate purely based on $R_{DS(on)}$; (c) Kalman filter estimation of $R_{DS(on)}$ resistance at reference temperature $T_{die} = 25\ °C$ and Kalman filter estimation of R_{th} resistance.

1) Estimation results: For the lab experiment, the same irradiance profile as in the simulation case is used. The resulting $R_{DS(on)}$ and R_{gate} resistance measurements are shown in Fig. 13a. The Kalman filter estimated T_{die} is given Fig. 13b. On the same figure a T_{die} estimate, purely based on the measured $R_{DS(on)}$ values is shown as well. It can be seen that the two estimates closely agree at the start after which they slowly drift apart as the degradation increases. Hence, $R_{DS(on)}$ alone becomes insufficient as temperature indicator. A difference of more than $10°C$ can be observed. The filter result of degradation indicators $R_{DS(on)}$ at reference temperature and R_{th} are given in Fig. 13c. Random initial values were used at the start of the algorithm. This leads to a transient which quickly converges to the actual estimated value, separated with a vertical dashed line. Smoothed curves are provided as dashed lines, giving the most likely trajectory. The RMSE on this fit of the $R_{DS(on)}$ and R_{th} trajectory is $81.9\ \mu\Omega$ and $68\ mW/K$ respectively. It can be seen that the $R_{DS(on)}$ increases during the experiment while R_{th} remains relatively constant after an initial setting of the thermal pad. This would mean that the component primarily experiences bond wire degradation. The setting of the thermal pad occurs because a phase change material is used which initially improves the thermal performance.

2) Estimation accuracy and degradation verification: Fig. 14a show the Kalman filter residual of T_{die} and $R_{DS(on)}$. It represents the difference between the output of the model and the instantaneous measurements, which is used to update the Kalman filter estimate. If the residual is big, the model is a bad representation of the actual system. Initially, the residual is expected to be large as the initial estimates of R_{th} and $R_{DS(on)}$ are not completely correct. Once the filter has migrated towards the correct values, the residual becomes small. Hence, the residual value is a good tool to identify the transient region, which is again indicated with a vertical dashed line. This region can be made smaller by increasing the plant variance. Notwithstanding, as degradation is a slow phenomena, it is often better to take the variance small, decreasing the noise on the estimate.

After the transient region, the error should be close to zero and only contain the noise which is filtered by the Kalman filter. Notwithstanding, some spikes can be noted in the residual signal, manly located in T_{die} at locations of high temperatures. These are clearly not solely related to noise and indicate an inconsistency between the model and the measured values. From the sensitivity analysis towards estimation errors, it became clear that mainly errors in the R_{gate} temperature dependency propagate in the output of the filter as the others only cause constant offsets. It is not surprising that this phenomenon occurs as the temperature measured using R_{gate} can be consistently incorrect by few degrees according to the confidence interval, even going up to $4\ °C$ at the highest temperatures. At the location of the main spike, a clearly erroneous dip can be observed in the estimated $R_{DS(on)}$, simultaneously with a local increase in the R_{th} estimate. This means that during these moments, the filter temporarily moves out of the confidence bounds of the measurements. Combining the deviation in the residual with the measurement error, the $95\ \%$ confidence interval widens to $5.6\ °C$ at these high temperatures. Outside if these regions, the filter output is expected to have the same confidence as the input measurements ($\pm 3.18\ °C$ and $\pm 2.0\ m\Omega$).

Next to this conceptual uncertainty propagation analysis, the estimated $R_{DS(on)}$ degradation can also be verified by measurement. To isolate the effect of degradation, all the measurement should be taken at the same temperature. To accomplish this, the irradiance levels in the valley of the profile were all put at exactly $250\ W/m^2$. Due to the limited amount of loss at this irradiance level, the changing thermal impedance has only a minor influence on the die temperature. Once the thermal capacitances of the component are discharged, the same die temperature is reached. This makes it possible to directly compare the measured $R_{DS(on)}$, which has a known confidence interval. Fig. 14b shows box-plots of the $R_{DS(on)}$ measurements in the different valleys, and it can be seen that it is increasing steadily such as the Kalman filter estimated. Verifying the trajectory of R_{th} is more difficult, as removing the component from the converter for additional measurement, significantly changes the actual R_{th}. Because of this, a more heuristic approach is taken. First, it can be stated that the observed trajectory is expected, seen the use of a phase change thermal pad. Next, the filter was successfully tested in simulation, and the input signals have a known and better accuracy. Last, the other $R_{DS(on)}$ output could be compared to measured values at fixed temperatures and proved to be accurate. Considering all of this, it is expected that also the R_{th} output lies close to the actual value. If not, the thermal model would be compromised, distorting the $R_{DS(on)}$ estimate as well.

C. Summary experimental results

An independent measurement was used to define the confidence bounds around the temperature dependencies observed by the input measurements. The amount of noise on the measurements was determined as well. The filter should be able to remove this noise and function correctly within the given confidence bounds. In the simulation study, it could be seen that the filters functions correctly under the presence of Gaussian noise. When estimations errors on the measurement temperature dependencies were introduced, R_{gate}

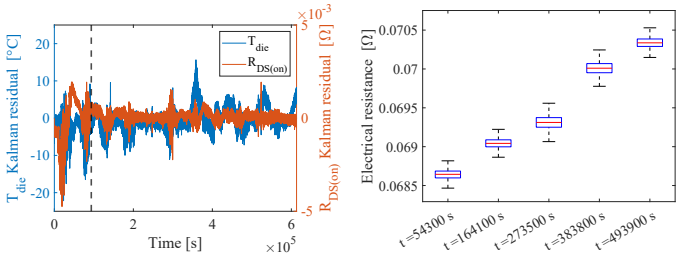

(a) (b)

Fig. 14: Accuracy indicators of the lab experiment: (a) Kalman filter residual signal of T_{die} and $R_{DS(on)}$; (b) Comparison of the $R_{DS(on)}$ measurement in the valley at different points in time.

proved to have the largest impact. In the lab experiment, the Kalman filter measured a steadily rising $R_{DS(on)}$ degradation and an almost constant R_{th} after an initial drop. When analyzing the filter residual, a few spikes are visible, indicating that in those regions the accuracy of the R_{gate} temperature is effecting the confidence of the filter output. This mainly happens at high temperatures. Besides these few regions, the filter is only removing noise and the output stays withing the confidence range of the input measurements. The $R_{DS(on)}$ could also be verified separately by measuring the resistance at constant operating conditions in the intervals.

V. Conclusion

Condition monitoring is an important technique to improve the reliability of power electronic systems. Temperature and damage sensitive parameters are often used for this purpose. The techniques demonstrated in current literature are only applicable in fixed mission profile applications. Other techniques that are suitable for varying mission profiles, neglect either the temperature or degradation related effects. This paper proposes a dual measurement approach, using the drain to source resistance and internal gate resistance to decouple mission profile temperature variations from the effects caused by degradation. Circuit implementations of the needed measurement circuits were shown together with the respective waveforms. The measurements signals are processed with a Dual Extended Kalman Filter, allowing to estimate both the die temperature and the changing drain to source and thermal resistance. It is shown that the needed thermal model can be conveniently extracted using a power step-response, obtaining the transient impedance curve. The Dual Extended Kalman Filter methodology was validated with both virtual and experimental data. The artificially generated test data showed that the correct values are extracted by the filter in presence of white noise. A sensitivity test was also conducted showing that estimation errors of the gate resistance temperature dependence have the largest impact on the estimation accuracy. Errors made in the estimated thermal model and drain to source on-resistance temperature dependence are automatically corrected by the filter. In a lab-test, the functioning of the measurement circuits was verified and the influence of temperature and degradation on the parameters was successfully decoupled. An emulated photovoltaic panel and maximum power point tracking algorithm made sure the converter was running in a realistic environment. This proofs that the methodology works in a practical setup and can be used to detect degradation in a power MOSFET. This paves the way for the implementation of control for reliability, this way relieving stress from the most critical components. It could also be utilized to schedule preventive maintenance, reducing outages and limiting the number of interventions needed.

Future work

In the introduction it was discussed that estimates of parameter degradation profiles can be included in the Kalman filter. This uses the knowledge that degradation can only rise which was not taken into account in the current implementation. The small variations which could be seen in the results could be eliminated this way. The disadvantage is that a specific degradation profile needs to be proposed which might deviate from the actual degradation profile.

As stated in the paper, it is possible to incorporate the non linear convective resistance in the state space, eliminating the need for the sink temperature measurement (if the ambient temperature is known). The increase in computational effort would be minimal as the Dual Extended Kalman Filter state space is already non-linear and needs to be linearized.

Another addition would be to include the electrical model in the state space. This way, the thermal model can be used to filter the R_{gate} measurement while the electrical model is used to filter the $R_{DS(on)}$ measurement. This could be beneficial as the $R_{DS(on)}$ measurement gets a worse signal over noise ratio at low current levels. The disadvantage of this approach is that additional electrical parameter measurements are needed as input for this electrical model. However, often some electrical parameters are already registered for converter control purposes as was the case in this work for the MPPT.

Further, it is also possible to take advantage from the different time scales of the two filters to reduce the computational intensity of this methodology. Because the parameters vary very slowly compared to the state, it is not necessary to evaluate the parameter Kalman filter at every time-step. An optimum can be found between the response speed of the parameters and the computational effort.

The current measurement circuits are a basic implementation to demonstrate the methodology. These circuits should be further refined to limit the losses caused by these circuits. An example are the relatively high shunt resistors used in the present designs.

As indicated, it is assumed that $R_{DS(on)}$ is purely dependent on degradation and die temperature. This was a good approximation for the device used in this work, however, this is not always the case. Most notably in the higher current ranges, some components show a considerable load current dependence. In future work this dependence could be included as well.

Lastly, the methodology could also be tested for devices other than Si MOSFETS, such as SiC and GaN switches. SiC generally uses similar packaging technologies for discrete devices and it is expected that this methodology can be directly applied. However, experimental validation is needed to provide certainty. GaN technology is still under development and a lot of new packaging types are introduced to cope with the high energy density and limit the parasitics to allow for extremely high switching speeds. As the proposed methodology is package specific, future research has to determine which adaptations are needed to perform condition monitoring on novel types of packages.

References

[1] S. Yang, A. Bryant, P. Mawby, D. Xiang, L. Ran, and P. Tavner, "An industry-based survey of reliability in power electronic converters," in *2009 IEEE Energy Conversion Congress and Exposition*. IEEE, sep 2009.

[2] M. Deckers, L. Van Cappellen, G. Emmers, F. Poormohammadi, and J. Driesen, "Cost comparison for different pv-battery system architectures including power converter reliability," in *2022 24th European Conference on Power Electronics and Applications (EPE'22 ECCE Europe)*, 2022, pp. 1–11.

[3] M. Deckers, S. Colnago, J. Driesen, and L. Piegari, "Influence of battery aging on converter switching device degradation," in *2023 IEEE 14th International Symposium on Diagnostics for Electrical Machines, Power Electronics and Drives (SDEMPED)*. IEEE, aug 2023.

[4] B. Wang, J. Cai, X. Du, and L. Zhou, "Review of power semiconductor device reliability for power converters," *CPSS Transactions on Power Electronics and Applications*, vol. 2, no. 2, pp. 101–117, 2017.

[5] Z. Ni, X. Lyu, O. P. Yadav, B. N. Singh, S. Zheng, and D. Cao, "Overview of real-time lifetime prediction and extension for sic power converters," *IEEE Transactions on Power Electronics*, vol. 35, no. 8, pp. 7765–7794, 2020.

[6] F. Yang, E. Ugur, and B. Akin, "Evaluation of aging's effect on temperature-sensitive electrical parameters in sic mosfets," *IEEE Transactions on Power Electronics*, vol. 35, no. 6, pp. 6315–6331, 2020.

[7] R. A. Bilir, N. Altintas, A. Bilir, E. Mese, and Z. Tosunoglu, "A comparative study on power mosfet reliability and failure modes," in *2019 18th International Symposium INFOTEH-JAHORINA (INFOTEH)*, 2019, pp. 1–5.

[8] H. Oh, B. Han, P. McCluskey, C. Han, and B. D. Youn, "Physics-of-failure, condition monitoring, and prognostics of insulated gate bipolar transistor modules: A review," *IEEE Transactions on Power Electronics*, vol. 30, no. 5, pp. 2413–2426, 2015.

[9] W. Kexin, D. Mingxing, X. Linlin, and L. Jian, "Study of bonding wire failure effects on external measurable signals of igbt module," *IEEE Transactions on Device and Materials Reliability*, vol. 14, no. 1, pp. 83–89, 2014.

[10] U.-M. Choi, F. Blaabjerg, and S. Jorgensen, "Power cycling test methods for reliability assessment of power device modules in respect to temperature stress," *IEEE Transactions on Power Electronics*, vol. 33, no. 3, pp. 2531–2551, 2018.

[11] M. H. M. Sathik, J. Pou, S. Prasanth, V. Muthu, R. Simanjorang, and A. K. Gupta, "Comparison of igbt junction temperature measurement and estimation methods-a review," in *2017 Asian Conference on Energy, Power and Transportation Electrification (ACEPT)*, 2017, pp. 1–8.

[12] F. Hosseinabadi, S. Jaman, S. K. Bhoi, M. M. Hasan, S. Chakraborty, M. El Baghdadi, and O. Hegazy, "Implementation of onsite junction temperature estimation for a sic mosfet module for condition monitoring," in *2022 24th European Conference on Power Electronics and Applications (EPE'22 ECCE Europe)*, 2022, pp. P.1–P.6.

[13] M. A. Eleffendi and M. Johnson, "Application of kalman filter to estimate junction temperature in igbt power modules," *IEEE Transactions on Power Electronics*, vol. 31, pp. 1–1, 03 2015.

[14] X. Han and M. Saeedifard, "Junction temperature estimation of sic mosfets based on extended kalman filtering," in *2018 IEEE Applied Power Electronics Conference and Exposition (APEC)*, 2018, pp. 1687–1694.

[15] K. Sharma, S. Kamm, K. M. Baron, and I. Kallfass, "Characterization of online junction temperature of the sic power mosfet by combination of four tseps using neural network," in *2022 24th European Conference on Power Electronics and Applications (EPE'22 ECCE Europe)*, 2022, pp. 1–8.

[16] M. M. Sathik, S. Prasanth, F. Sasongko, and J. Pou, "Online condition monitoring of IGBT modules using current-change rate identification," *Microelectronics Reliability*, vol. 92, pp. 55–62, jan 2019.

[17] Y. Peng, S. Zhao, and H. Wang, "A digital twin based estimation method for health indicators of dc-dc converters," *IEEE Transactions on Power Electronics*, vol. 36, no. 2, pp. 2105–2118, 2021.

[18] J. Celaya, A. Saxena, S. Saha, and K. Goebel, "Prognostics of power mosfets under thermal stress accelerated aging using data-driven and model-based methodologies," *Proceedings of International Conference on Prognostics and Health Management, Montreal*, vol. 2, 01 2011.

[19] S. Dusmez, H. Duran, and B. Akin, "Remaining useful lifetime estimation for thermally stressed power mosfets based on on-state resistance variation," *IEEE Transactions on Industry Applications*, vol. 52, no. 3, pp. 2554–2563, 2016.

[20] A. Alyakhni, A. Al-Mohamad, and G. Hoblos, "Joint estimation of mosfet degradation in a dc-dc converter using extended kalman filter," in *2019 4th Conference on Control and Fault Tolerant Systems (SysTol)*, 2019, pp. 319–324.

[21] X. Sun, M. Huang, Y. Liu, and X. Zha, "Investigation of artificial neural network algorithm based IGBT online condition monitoring," *Microelectronics Reliability*, vol. 88-90, pp. 103–106, sep 2018.

[22] U. Choi, F. Blaabjerg, and F. Iannuzzo, "Advanced power cycler with intelligent monitoring strategy of IGBT module under test," *Microelectronics Reliability*, vol. 76-77, pp. 522–526, sep 2017.

[23] B. Rannestad, P. Nielsen, S. Munk-Nielsen, K. Gadgaard, and S. Jorgensen, "Converter monitoring in a wind turbine application," *Microelectronics Reliability*, vol. 88-90, pp. 1008–1013, sep 2018.

[24] S. Dan, *Optimal State Estimation*. John Wiley and Sons, Ltd, 2006.

[25] S. Haykin, *Kalman Filtering and Neural Networks*. John Wiley and Sons, Ltd, 2001, ch. 1, pp. 1–21.

[26] C. Li, Y. Liu, L. Sun, Y. Liu, M. Tomizuka, and W. Zhan, "Dual extended kalman filter based state and parameter estimator for model-based control in autonomous vehicles," in *2021 IEEE International Intelligent Transportation Systems Conference (ITSC)*, 2021, pp. 327–333.

[27] L. Van Cappellen, M. Deckers, O. Alavi, M. Daenen, and J. Driesen, "A real-time physics based digital twin for online mosfet condition monitoring in pv converter applications," in *2022 28th International Workshop on Thermal Investigations of ICs and Systems (THERMINIC)*, 2022, pp. 1–4.

[28] T. Lopez and R. Elferich, "Thermal impedance extraction technique for power mosfets," in *2007 IEEE Power Electronics Specialists Conference*, 2007, pp. 2140–2146.

[29] *MOSFET Power Losses Calculation Using the Data-Sheet Parameters*, Infineon, 7 2006, v 1.1.

[30] R. Gelagaev, P. Jacqmaer, and J. Driesen, "A fast voltage clamp circuit for the accurate measurement of the dynamic on-resistance of power transistors," *IEEE Transactions on Industrial Electronics*, vol. 62, no. 2, pp. 1241–1250, 2015.

[31] A. Koenig, T. Plum, P. Fidler, and R. W. De Doncker, "On-line junction temperature measurement of coolmos devices," in *2007 7th International Conference on Power Electronics and Drive Systems*, 2007, pp. 90–95.

[32] P. Ghimire, A. R. de Vega, S. Beczkowski, B. Rannestad, S. Munk-Nielsen, and P. Thogersen, "Improving power converter reliability: Online monitoring of high-power igbt modules," *IEEE Industrial Electronics Magazine*, vol. 8, no. 3, pp. 40–50, 2014.

[33] K. M. Baron, K. Sharma, M. Nitzsche, and I. Kallfass, "Online monitoring of degradation sensitive electrical parameters in inverter operation for sic-mosfets," in *2021 IEEE Applied Power Electronics Conference and Exposition (APEC)*, 2021, pp. 1235–1241.

[34] M. Denk and M.-M. Bakran, "Comparison of uce- and rgi-based junction temperature measurement of multichip igbt power modules," in *2015 17th European Conference on Power Electronics and Applications (EPE'15 ECCE-Europe)*, 2015, pp. 1–11.

[35] N. Baker, S. Munk-Nielsen, F. Iannuzzo, and M. Liserre, "Online junction temperature measurement using peak gate current," in *2015 IEEE Applied Power Electronics Conference and Exposition (APEC)*, 2015, pp. 1270–1275.

[36] M. Maerz and P. Nance, "Thermal modeling of power electronic systems," *PCIM Europe Mag*, vol. 2, 02 2000.